CERN–PPE/95-162
16. November 1995

Isotope Effects on Delayed Annihilation Time Spectra of Antiprotonic Helium Atoms in Low Temperature Gas

B. Ketzer[1)], F. J. Hartmann[1)], H. Daniel[1)], T. von Egidy[1)], A. Niestroj[1)], S. Schmid[1)], W. Schmid[1)], T. Yamazaki[2)], I. Sugai[2)], K. Nakayoshi[2)], R. S. Hayano[3)], F. E. Maas[3)], H. A. Torii,[3)] T. Ishikawa[3)], H. Tamura[3)], N. Morita[4)], D. Horváth[5)], J. Eades[6)], E. Widmann[6)]

PS205 collaboration

Abstract

The delayed annihilation time spectra (DATS) of antiprotonic helium atoms have been studied in isotopically pure low temperature ^{3}He and ^{4}He gas at various densities. The DATS taken at 5.8 K and 400 mbar are very similar in shape except for i) a small difference in the time scale and ii) the presence of a distinct fast decay component in the case of ^{3}He. The ratio of overall trapping times (mean lifetimes against annihilation), $R = T_{\rm trap}(^4{\rm He})/T_{\rm trap}(^3{\rm He})$, has been determined to be 1.144 $\pm$ 0.009, which is in good agreement with a theoretical estimate yielding $R = [(M^*(\overline{\rm p}^4{\rm He})/M^*(\overline{\rm p}^3{\rm He})]^2$=1.14, where M^* denotes the reduced mass of the $\overline{\rm p}{\rm He}^{++}$ system. The presence of a short-lived component with a lifetime of (0.154 ± 0.007) μs in the case of ^{3}He suggests that the $\overline{\rm p}^3{\rm He}^+$ atom has a state of intermediate lifetime on the border between a metastable zone and an Auger-dominated short-lived zone. The fraction of antiprotons trapped in metastable states at 5.8 K and 400 mbar is lower by $22.2(4)\%$ for ^{3}He than for ^{4}He. All the data can be fitted fairly well with simple 3-level and 4-level cascade models.

Submitted to Physical Review A

PACS 36.10.-k

[1)] Physik-Department, Technische Universität München, D-85747 Garching, Germany
[2)] Institute for Nuclear Study, University of Tokyo, 3-2-1 Midori-cho, Tanashi, Tokyo 188, Japan
[3)] Department of Physics, University of Tokyo, 7-3-1 Hongo, Bunkyo-ku, Tokyo 113, Japan
[4)] Institute for Molecular Science, Myodaiji, Okazaki 444, Japan
[5)] KFKI Research Institute for Particle and Nuclear Physics, H-1525 Budapest, Hungary
[6)] CERN, CH-1211 Geneva 23, Switzerland

1 Introduction

The discovery of the delayed annihilation of antiprotons in liquid helium at the Japanese National Laboratory for High Energy Physics, KEK, in 1991 [1] contradicted the long-standing belief that every antiproton coming to rest in matter would annihilate with the nucleus within picoseconds. About three percent of all antiprotons stopped in liquid helium were found to survive for an average lifetime of 3 μs, some of them living as long as 25 μs — more than seven orders of magnitude above the expected value. The historical background is reviewed in [2].

The first experiment at LEAR/CERN in November 1991 confirmed this longevity in gaseous ^{3}He and ^{4}He at room temperature, and revealed also a different mean lifetime of the long-living antiprotons in the two helium isotopes [3, 4]. This isotope effect had previously been postulated by Yamazaki and Ohtsuki [5] on the basis of a $\overline{\mathrm{p}}\mathrm{He}^+$ model suggested by Condo [6] and developed by Russell [7]. According to this model a metastable $\overline{\mathrm{p}}\mathrm{He}^+$ atom results when the antiproton is captured into nearly circular states with high principal quantum number

$$n \sim n_0 \equiv \sqrt{M^*/m_e} \tag{1}$$

and high angular momentum quantum number $l \leq n-1$. Depending on the reduced mass M^* of the $\overline{\mathrm{p}}\mathrm{He}^{++}$ system, n_0 is 38 for $\overline{\mathrm{p}}^4\mathrm{He}^+$ and 37 for $\overline{\mathrm{p}}^3\mathrm{He}^+$. The small energy spacing of levels with $\Delta n = 1$ in this region ($\sim$ 2 eV) strongly suppresses internal and external Auger deexcitation, since an energy of at least 25 eV is necessary for electron emission. The continued electron presence removes the l degeneracy of antiproton states with equal n. At the same time the electron provides a Pauli-repulsion effect during collisions with other helium atoms. Both these effects strongly reduce the collisional Stark mixing to nS states, which normally produces immediate annihilation. The only remaining deexcitation processes are slow radiative transitions. The joint effect of all these circumstances is to produce the anomalously long antiproton lifetimes observed.

In November 1992 further extensive measurements of delayed annihilation time spectra (DATS) from low temperature ^{4}He gas, high pressure liquid ^{3}He and ^{4}He and solid ^{4}He were carried out, which yielded important results on the phase and density dependence of DATS from pure helium media [8]. The isotope effect seen previously in room temperature gases [4] was found to occur in the liquid phase also. In liquid ^{4}He the lifetime gradually became shorter with increasing density and a distinct fast component was observed. The DATS from low temperature ^{4}He gas showed the longest $\overline{\mathrm{p}}$ lifetime ($\sim$ 4 μs) and no fast decaying component. These observations prompted us to look for a similar isotope effect in low temperature gas.

In the present paper we report the results of precise measurements of DATS from low temperature ^{3}He and ^{4}He gases. Here, we employed a new method using a highly efficient detection system for annihilation pions (both charged and neutral), which was designed and developed for laser resonance experiments [9, 10].

After a brief account of the experimental setup in Sec. II the experimental results are presented in Sec. III. Section IV introduces some models to reproduce the characteristic shape of the time spectra. In Sec. V the experimental results rea discussed and compared with theoretical accounts.

2 Experimental Method

The complete experimental setup used in the present experiment (including the high efficiency detection system and the cryostat used to provide the low temperature gas target) will be described in a forthcoming publication [11]. Here we confine ourselves to a brief description of the setup, the electronics and the data acquisition system necessary to record the time spectra.

2.1 Experimental Arrangement

Figure 1 shows a plan view of the setup used in the experiments for investigating the long-lived states in $\overline{\mathrm{p}}\mathrm{He}^+$ atoms. A 200 MeV/c $\overline{\mathrm{p}}$ beam with an intensity of about 10^4 $\overline{\mathrm{p}}$ s^{-1} was delivered from the Low Energy Antiproton Ring LEAR at CERN. At the end of the beam line, the antiprotons passed through a 100 μm thick Be window into the air and then traversed a 0.5 mm thick plastic scintillator, which served as a beam counter to provide the start signal for the annihilation time measurements. After passing through the hole in a ring veto counter (A), the antiprotons entered the helium target chamber through 50 μm Kapton and 407 μm steel windows, the latter being covered with an 875 μm thick Euplex foil (similar to Kapton) for moderation, a value which was determined by Monte Carlo simulation. Details on this program, which takes into account the Barkas effect of the energy loss, can be found in [4]. A CCD camera with its optical axis at 45° to the beam axis imaged scintillation light leaking out of the surface of the beam counter B and allowed us to monitor the beam position [12]. An additional 50 μm thick degrader (Euplex foil) was placed in front of the Kapton window to fine tune the stopping distribution of antiprotons in the target gas.

Annihilation time spectra were recorded in isotopically pure gaseous ^{4}He (impurity content < 1 ppm) and ^{3}He (enrichment 99.95%, impurity content < 30 ppm) at pressures between 200 mbar and 1040 mbar and low temperatures, since the longest $\overline{\mathrm{p}}$ lifetimes have been observed under these conditions [8].

The cryostat used to cool the target gas to temperatures between 4.3 K and 10 K resembled the one used in previous experiments discussed in [8]: the cylindrical target chamber was 21.8 cm long and had a diameter of 6.2 cm. Liquid helium from a reservoir evaporated into a second chamber surrounding the target chamber, the flow of helium being controlled by a needle valve. The fine adjustment of the temperature was carried out via a heating wire located at the vaporizer and connected in a feedback loop to a temperature sensor in contact with the target vessel.

Charged pions and π^0 decay gammas from antiproton annihilation were detected in seven shower counters (S in Fig. 1), each comprising 11 layers of alternating scintillator and lead plates. These counters, subtending a solid angle of about 80% of 4π, were able to detect annihilation events with an efficiency of about 99.7%.

2.2 Electronics

The logic diagram of the electronics is shown in Fig. 2. Light from the beam counter B was detected by two photomultipliers on opposite sides of the scintillator. The signals of the seven shower counters are represented by S0 through S6. A wide range TDC (LeCroy 4208) with a resolution of 1ns/channel was used for the timing measurements. The coincidence of the beam detectors B1 and B2 started all the TDC channels if the antiproton had not hit the veto counter A, if the computer was not busy with readout and if no $\overline{\mathrm{p}}$ had been detected by either A, B1 or B2 within the previous 50 μs. Each shower counter signal S0. . .S6 stopped a different TDC channel. The trigger condition for computer readout of an event was

$$\mathrm{B1} \times \mathrm{B2} \times \overline{\mathrm{A}} \times \overline{\text{Computer Veto}} \times \overline{\text{Pre Pile Up}} \times \sum_{i=0}^{6} \mathrm{S}_i,$$

where $\sum_{i=0}^{6} \mathrm{S}_i$ is the analog sum of the shower counter signals. The time spectra were recorded in the range from -0.5 μs to $+49.5$ μs relative to the time of the prompt annihilation peak by delaying the stop signals by ~ 500 ns. Prompt annihilation events could be discarded by the electronics ('prompt veto'), thus considerably reducing the computer dead time. To avoid confusion in assigning annihilation events to the corresponding antiprotons, pre pile-up events (those in

which a $\overline{\mathrm{p}}$ had been detected within the previous 50 μs) were rejected by hardware veto, as described above. Post pile-up events (events with a second $\overline{\mathrm{p}}$ within 50 μs after TDC start), on the other hand, had to be discarded in the analysis. For that purpose the time spectra of the beam detectors B1 and B2 were recorded using the multi-hit mode of the TDC (in which the time interval between two successive pulses in the same input line is digitized). If the spectrum of one of the B counters had multiple hits within the time window of 50 μs the event was discarded by software.

For each event the TDC information as well as the analog signals of all detectors were stored. The data were acquired by a CES Starburst J11, a PDP-11 compatible CAMAC Auxiliary Controller, transferred to a VAX station using Direct Memory Access and then written on tape. Since we carried out pre and post pile-up rejection in an interval of 50 μs each, the dead time of the data acquisition system was ~ 100 μs per accepted event.

2.3 Data Analysis

The data were analyzed event by event as follows:

1. Post pile-up events were rejected using the multihit mode of the TDC.
2. The annihilation time and the time spread of the shower counter hits were calculated.
3. Events with only a single hit on one of the seven shower counters were discarded.

The post pile-up rejection has already been described in the previous section. The annihilation time is defined as the time between passage of the $\overline{\mathrm{p}}$ through detector B and the average time of arrival of its annihilation products in the shower counters. Only events for which the standard deviation of the shower counter events from their average was less than 10 ns were included ('dispersion' cut). To minimize the background caused by $\pi^+ \rightarrow \mu^+ \rightarrow \mathrm{e}^+$ decays, we required that at least two of the seven shower counters had detected an annihilation product ('multiplicity two' cut)

3 Experimental Results

Figure 3 shows two typical DATS from ^{4}He and ^{3}He, both taken at 5.8 K and 400 mbar. The time spectrum from ^{4}He is essentially the same as our previous one [3, 4, 8], but with better statistics and background suppression, showing again that antiprotons can survive up to 25 μs in helium gas. Both DATS clearly deviate from a single exponential slope, exhibiting a downward bent structure for long decay times when plotted in a logarithmic scale. This shape indicates that the $\overline{\mathrm{p}}$ cascades down a ladder of successive metastable levels, before coming to a state from where a fast Auger transition is possible. Annihilation via the Stark effect in a collision with another helium atom then immediately follows the ejection of the remaining electron. Although the maximum trapping time of an antiproton in ^{4}He is clearly longer than in ^{3}He, the DATS from ^{3}He and ^{4}He are very similar in shape for $t > 2$ μs. For shorter decay times, however, a distinct fast component shows up in ^{3}He, but not in ^{4}He.

Tables 1 and 2 summarize the experimental conditions and results for low temperature pure ^{3}He and ^{4}He measurements. The molar density ϱ_{mol} was calculated using the second order virial expansion of the state equation. The second virial coefficients for ^{3}He and ^{4}He were interpolated from theoretical values [13]. The trapping fraction f, the average lifetime T_{av} of antiprotons and the results of fitting cascade models to the time spectra, shown in the subsequent columns, will be discussed in the following sections.

3.1 Trapping Fraction

The trapping fraction f, defined as

$$f = \frac{\text{Number of delayed annihilations}}{\text{Total number of annihilations}}, \tag{2}$$

is only given for runs in which the prompt peak had not been suppressed by the electronic prompt veto. An annihilation was then considered as delayed if it occured more than 15 ns after arrival of the antiproton. In Fig. 4 the experimental results for f in ^{3}He and ^{4}He, shown in Tables 1 and 2, are plotted versus the molar density. The trapping fraction in ^{3}He is always significantly lower than that in ^{4}He. At 5.8 K and 400 mbar the observed ratio is

$$\frac{f(^3\text{He})}{f(^4\text{He})} = 0.778 \pm 0.004. \tag{3}$$

With the exception of very low densities it remains constant in the density region under investigation.

The scintillation counter array used in previous experiments [4, 8] was able to distinguish between annihilations in the target gas and in the walls of the target chamber. This feature was lost in the highly efficient shower counter system described in Sec. II. Antiprotons annihilating in the target chamber walls, however, would contribute to the prompt peak and would therefore bias the result for the trapping fraction. To investigate this problem, we calculated the stopping distribution of antiprotons in our target by Monte Carlo simulation [4]. Figure 5 a) shows the stopping distribution of 10000 $\overline{\text{p}}$ (200 MeV/c) obtained in ^{4}He gas at a temperature of 5.8 K and a pressure of 400 mbar ($\varrho_{\text{mol}} = 8.66 \cdot 10^{-4}$ mol/cm^3). The fraction of $\overline{\text{p}}$ stopping in the walls of the target chamber under these conditions is only about 1.1% and is not sensitive to possible uncertainties of the thicknesses of counters and windows in the beamline. The antiprotons were calculated to have a mean range of 8.6 cm and a range straggling of 3.6 cm (FWHM) in the target cell. The situation changes drastically when the pressure is decreased to 200 mbar (Fig. 5 b). According to our simulation the mean range of antiprotons in the target gas at these conditions is 16.9 cm, with a range straggling of 9.5 cm (FWHM). About 50% of the antiprotons were then found to annihilate in the walls of the target chamber, thus considerably reducing the fraction of delayed $\overline{\text{p}}$. Unlike the situation at 400 mbar, however, this number depends strongly on the exact thicknesses of counters and windows in the beamline. Nevertheless, the simulation clearly shows that most antiprotons are stopped inside the target at 5.8 K and 400 mbar. We therefore use the data at our experimental 'standard' conditions, namely 5.8 K and 400 mbar.

3.2 Overall Trapping Time

Figure 6 a) compares DATS from pure ^{3}He and ^{4}He at 5.8 K and 400 mbar, showing that the shapes of the spectra after 2 μs are surprisingly similar to each other except for the time scale. A quantitative value for this difference can be obtained by enlarging the time scale of the ^{3}He spectrum, until the long-lived parts of the two spectra match [4]. In order not to be sensitive to different short-lived components, only the time range between 2 μs and 17.5 μs was taken into account. Figure 6 b) shows the same spectra as Fig. 6 a), with the time scale of the ^{3}He spectrum stretched by 14.6% (solid line) and the ^{4}He spectrum containing the errors of both spectra. From various pairs of DATS taken at the same conditions we obtained an average scaling factor of 1.144, which is readily interpreted as the ratio of overall trapping times

$$\frac{T_{\text{trap}}(^4\text{He})}{T_{\text{trap}}(^3\text{He})} = 1.144 \pm 0.009. \tag{4}$$

In previous publications [4, 8] the average lifetime T_{av} of antiprotons, calculated from the time spectra $N(t)$ as

$$T_{\mathrm{av}}(t_0, t_{\mathrm{max}}) = \frac{\int_{t_0}^{t_{\mathrm{max}}} t \cdot N(t)\,\mathrm{d}t}{\int_{t_0}^{t_{\mathrm{max}}} N(t)\,\mathrm{d}t} - t_0, \tag{5}$$

has been used to compare DATS from ^{3}He and ^{4}He. In order to consider only the long-lived part of the spectra, t_0 was chosen to be 2 μs for ^{3}He and ^{4}He. For a fair comparison of $T_{\mathrm{av}}(^3\mathrm{He})$ and $T_{\mathrm{av}}(^4\mathrm{He})$, however, one has to take into account that the time scale for ^{4}He was found to be a factor of 1.144 larger than for ^{3}He. If t_0 is set to be 2 μs for ^{3}He, a value of $t_0 = 1.144 \cdot 2\ \mu\mathrm{s} \simeq 2.3\ \mu\mathrm{s}$ should therefore be used for ^{4}He. Table 1 shows $T_{\mathrm{av}}(^3\mathrm{He})$, calculated for $t_0 = 2\ \mu$s, while Table 2 contains $T_{\mathrm{av}}(^4\mathrm{He})$ for $t_0 = 2.3\ \mu$s. At 'standard' conditions the ratio of average lifetimes in ^{4}He and ^{3}He is

$$\frac{T_{\mathrm{av}}(^4\mathrm{He})}{T_{\mathrm{av}}(^3\mathrm{He})} \simeq 1.153 \pm 0.009, \tag{6}$$

showing that T_{av} indeed reflects the overall trapping time of antiprotons, provided that the different time scales in ^{3}He and ^{4}He are taken into consideration.

3.3 Short-lived Component

Apart from the small difference in the long-living part of the spectra a strong fast decaying component appears in all ^{3}He DATS, which is not present in low density ^{4}He (Fig. 3). Although small admixtures of foreign gases (in particular H_2 and O_2) to helium are known to induce a fast component in the spectra [14], there is no possibility that gaseous impurities introduced into the present target could have caused the short-lived component in ^{3}He alone, because at temperatures around 5 K all possible impurities, e.g. H_2 or O_2, are frozen or liquefied. The presence of the fast decaying component is therefore intrinsic to ^{3}He. By fitting a simple sum of two exponential functions to the ^{3}He spectra between 0.1 μs and 5 μs, the lifetime of the fast component in ^{3}He was determined to be $(0.154 \pm 0.007)\ \mu$s. The fraction of all trapped antiprotons annihilating with this relatively short lifetime (compared to radiative transitions) was found to be $(13.3 \pm 0.2)\%$. This suggests that there is at least one state in $\overline{\mathrm{p}}^3\mathrm{He}^+$, which has an intermediate lifetime between metastability (lifetime $\sim$ 1–2 μs) and Auger-dominance (lifetime $\leq$ 10 ns).

4 Fitting to Cascade Models

In the previous section the various overall trapping times of antiprotons in ^{3}He and ^{4}He have been determined by comparing DATS from ^{3}He and ^{4}He from 2 μs up. These methods, with their sensitivity limited to the long-lived region, do not take into account the different short-lived components in ^{3}He and ^{4}He. We therefore tried to find a fitting function which is capable of describing both the short- and long-lived components in the DATS. A propensity rule implies that, after being captured into a metastable state, the antiprotons follow a cascade through subsequent metastable levels with $\Delta n = \Delta l = -1$ [5, 15]. The DATS we observe are therefore a superposition of almost independent sequences, each with a radial node number $v = n - l - 1 = \mathrm{const}$. The ratio of crossover transitions between individual sequences have been estimated to be at least one order of magnitude smaller than the radiative transitions within a given chain [5]. As an approximation, one may describe the system of independent sequences by only one (fictitious) representative ladder of levels, averaging over the individual cascades.

4.1 Three-Level Cascade Model

The simplest model which is able to reproduce the characteristic downward bending of the annihilation spectra at $t \sim 8\ \mu$s is a $\overline{\mathrm{p}}$ cascade over three metastable levels followed by an Auger-dominated short-lived state [8], as shown in Fig. 7. The antiproton annihilates immediately after

the fast Auger transition to an ionized $\overline{\mathrm{p}}\mathrm{He}^{++}$ state. The rate equations for the populations of the different levels are then

$$\frac{\mathrm{dN}_1}{\mathrm{dt}} = -\lambda_1 N_1, \tag{7}$$

$$\frac{\mathrm{dN}_2}{\mathrm{dt}} = -\lambda_2 N_2 + \lambda_1 N_1, \tag{8}$$

$$\frac{\mathrm{dN}_3}{\mathrm{dt}} = -\lambda_3 N_3 + \lambda_2 N_2, \tag{9}$$

with λ_i being the radiative decay rates of the metastable states. Since our aim was only to reproduce the gross shape of the time spectra from 100 ns on, the Auger-dominated state at the end of the cascade was not taken into account in our models. Due to the non-orthogonality of real exponential functions it is difficult to obtain a consistent set of fit results with six free parameters. In most of the cases, however, we found similar values for the radiative rates λ_1 and λ_2 both in ^{3}He and ^{4}He. Therefore we set $\lambda_1 = \lambda_2$ and further assumed that the initial populations of all three levels be equal ($N_1(0) = N_2(0) = N_3(0) \equiv N_0$). In view of the high level-density and the small level-spacing around $n = n_0$ this is probably justified. The solution for $N_3(t)$ of this system of differential equations with three free parameters is

$$\begin{aligned} N_3(t) = {} & N_0 \left\{ \frac{\lambda_1^2 t}{\lambda_3 - \lambda_1} - \frac{\lambda_1^2}{(\lambda_3 - \lambda_1)^2} + \frac{\lambda_1}{\lambda_3 - \lambda_1} \right\} e^{-\lambda_1 t} \\ & + N_0 \left\{ 1 - \frac{\lambda_1}{\lambda_3 - \lambda_1} + \frac{\lambda_1^2}{(\lambda_3 - \lambda_1)^2} \right\} e^{-\lambda_3 t}. \end{aligned} \tag{10}$$

Figure 8 shows the results of a fit of the annihilation rate $\lambda_3 N_3(t)$ to typical spectra, recorded at 5.8 K and 400 mbar in ^{3}He and ^{4}He. The shape of DATS from ^{4}He without a fast component is described satisfactorily ($\chi^2_{\mathrm{red}} \sim 2$), while the simplified 3-level fitting function cannot reproduce the strong short-lived component *and* the downward bent structure of $\ln N(t)$ for longer decay times in ^{3}He ($\chi^2_{\mathrm{red}} \sim 10$). Despite this lack of sensitivity the fit results for λ_1 and λ_3 are presented in Tables 1 and 2 for comparison with earlier publications. The 6-parameter fit provides a better representation of ^{3}He DATS, but, as mentioned above, the fit results are inconsistent due to the large number of free parameters.

4.2 Four-Level Cascade Model

One obvious possibility to enhance the growth-decay structure of the fitting function necessary for satisfactory fit results for ^{3}He, is to consider a $\overline{\mathrm{p}}$ cascade over four metastable states instead of three, as shown in Fig. 9. Since the downward bent shape of the DATS indicates a reduced feeding from higher levels at longer decay times, the initial population N_0^1 of the highest state in this four-level decay chain was introduced as an additional free parameter in the fit. The initial populations of the lower levels were assumed to be equal (N_0). To ensure stable fit results, the decay rates were set to be equal for the three upper levels, as in the three-level model. Extending the three-level model as described results in a second growth-decay term $\propto t^2 e^{-\lambda_1 t}$ in addition to the one $\propto t e^{-\lambda_1 t}$ in Eq. 10:

$$\begin{aligned} N_4(t) = {} & \left\{ N_0^1 \frac{\lambda_1^3 t^2}{2(\lambda_4 - \lambda_1)} - N_0^1 \frac{\lambda_1^3 t}{(\lambda_4 - \lambda_1)^2} + N_0 \frac{\lambda_1^2 t}{\lambda_4 - \lambda_1} \right\} e^{-\lambda_1 t} \\ & + N_0 \left\{ \frac{\lambda_1^3}{(\lambda_4 - \lambda_1)^3} - \frac{\lambda_1^2}{(\lambda_4 - \lambda_1)^2} + \frac{\lambda_1}{\lambda_4 - \lambda_1} \right\} e^{-\lambda_1 t} \\ & + N_0 \left\{ 1 - \frac{\lambda_1}{\lambda_4 - \lambda_1} + \frac{\lambda_1^2}{(\lambda_4 - \lambda_1)^2} - \frac{\lambda_1^3}{(\lambda_4 - \lambda_1)^3} \right\} e^{-\lambda_4 t}. \end{aligned} \tag{11}$$

Typical fits are presented in Fig. 10. The function is capable of reproducing the behaviour of DATS from ^{4}He (a) and ^{3}He (b) both for short and long decay times ($\chi^2_{\rm red} \sim 2$). To achieve this, however, an additional parameter had to be introduced.

The results for λ_1 and λ_4 are given in Tables 1 and 2. In Fig. 11 the radiative rates λ_1, λ_4 and the ratio of initial populations N_0^1/N_0 are plotted versus the molar density. The decay rate λ_1 of the upper metastable states was found to be higher for ^{3}He than for ^{4}He (Fig. 11 a). Comparing values of λ_1 for ^{3}He and ^{4}He at 'standard' conditions one finds an average ratio of

$$\frac{\lambda_1(^3\mathrm{He})}{\lambda_1(^4\mathrm{He})} \simeq 1.14 \pm 0.03, \tag{12}$$

which is in good agreement with the ratio we have obtained from the direct comparison of DATS (Eq. 4). Thus, λ_1 determines the overall trapping time in our model. It is interesting to see that the value of λ_1 found for ^{4}He ($0.46(1)\ \mu\mathrm{s}^{-1}$) in such a simplified model is in agreement with the decay rate of the $(n,l) = (40,36)$ state ($0.49(2)\ \mu\mathrm{s}^{-1}$), determined by resonant deexcitation of antiprotons with laser light [10].

The decay rate of the last metastable level λ_4 in our model represents the fast decaying component of DATS (Fig. 11 b): it is roughly a factor of three higher in ^{3}He than in ^{4}He, again suggesting the existence of at least one border state with a lifetime between a metastable and an Auger-dominated zone in ^{3}He. However, no calculations of Auger rates have been performed for ^{3}He up to now. Again, the result for λ_4 in ^{4}He ($0.78(2)\ \mu\mathrm{s}^{-1}$) agrees surprisingly well with the value found for the state $(n,l) = (39,35)$ in our laser resonance experiment ($0.72(2)\ \mu\mathrm{s}^{-1}$).

The ratio of initial populations N_0^1/N_0, presented in Fig. 11 c), is in all cases smaller than unity, indicating that the initial population of metastable states in a $\overline{\mathrm{p}}$ He$^+$ atom decreases with increasing principal quantum number n. Several theoretical arguments based on calculated transition rates show that an artificial cutoff in the initial population of states above $n \sim 40$ is necessary to reproduce the shape of DATS [16, 17].

5 Discussion and Conclusions

The observed isotope effects have to be compared with the present theoretical knowledge of $\overline{\mathrm{p}}$He$^+$ atoms. The two main theoretical descriptions of this three-body system are the molecular approach [15, 18, 19] and the atomic approach [5]. Very recently they have been supplemented by large configuration-space variational methods [20], which yielded the energy levels and transition energies shown in Fig. 12. The rates for radiative transitions have been calculated both in the molecular and the atomic approaches. $\overline{\mathrm{p}}^4$He$^+$ and $\overline{\mathrm{p}}^3$He$^+$, as shown in Up to now, the Auger rates have only been calculated for $\overline{\mathrm{p}}^4$He$^+$, using the atomic model [5]. According to these calculations, Auger transitions with $\Delta l \leq 3$ to states of ionized $\overline{\mathrm{p}}$He^{++} (also shown in Fig. 12) occur quickly, the relevant states having lifetimes ≤ 10 ns (indicated by zigzag lines in Fig. 12). Auger transitions with $\Delta l > 3$, on the other hand, are expected to be much slower even than the radiative processes and are thus 'forbidden'. The corresponding metastable levels have lifetimes in the order of 1–2 μs (indicated by bold lines in Fig. 12). While actually calculated only for $\overline{\mathrm{p}}^4$He$^+$, the same rule was applied to the case of $\overline{\mathrm{p}}^3$He$^+$ in Fig. 12 b).

The overall trapping time $T_{\rm trap}$ of antiprotons depends on i) the lifetimes of the individual metastable levels, ii) the number of metastable states and iii) the initial population of these states. Assuming that the $\overline{\mathrm{p}}$ is captured into a Bohr orbit with a principal quantum number $n \sim n_0 = \sqrt{M^*/m_{\rm e}}$ (approximately 38 for ^{4}He and 37 for ^{3}He) and with a lifetime τ_{n_0}, the overall trapping time $T_{\rm trap}$ can be estimated [5] by

$$T_{\rm trap} \propto \tau_{n_0} \times \text{Number of metastable states} \propto \left[\frac{M^*}{m_{\rm e}}\right]^{3/2} \cdot \left[\frac{M^*}{m_{\rm e}}\right]^{1/2} = \left[\frac{M^*}{m_{\rm e}}\right]^2. \tag{13}$$

This yields for the ratio of overall trapping times in ^{4}He and ^{3}He

$$\frac{T_{\rm trap}(^4{\rm He})}{T_{\rm trap}(^3{\rm He})} \approx \left[\frac{M^*(\overline{\rm p}^4{\rm He})}{M^*(\overline{\rm p}^3{\rm He})}\right]^2 \simeq 1.14. \qquad (14)$$

The experimental results for this ratio, as given in Eqs. 4 and 6, are in excellent agreement with this simple theoretical consideration based on the atomic model. A less direct approach to compare the DATS from ^{4}He and ^{3}He is to examine the fitted decay rates. The ratio we obtain from values of λ_1 found in the four-level model for ^{3}He and ^{4}He at similar densities (Eq. 12) shows that λ_1 determines the overall trapping time in our model. We cannot extract decay rates of individual states from these simplified models, for which the ratio of lifetimes according to Eq. 13 would be 1.10. Therefore, we have shown that the three different methods employed — scaling of the spectra, calculating the average lifetime and fitting a chain decay model — converge to the same result for the overall trapping time as a simple theoretical estimate.

The fact that we have observed a pronounced short-lived component in ^{3}He DATS at 5.8 K and 400 mbar, which does not appear in ^{4}He under the same conditions, seems to indicate the existence of an initially populated state with an intermediate lifetime between the metastable zone and the Auger-dominated zone in ^{3}He. Calculations of Auger-transition rates for ^{3}He, which might give an explanation for this striking effect, are therefore eagerly awaited.

We have observed a 22% lower trapping fraction of antiprotons in pure ^{3}He than in pure ^{4}He at low temperatures. A similar difference of the trapping fractions in room temperature gases was also reported in [4]. On the other hand, a crude theoretical estimate assuming a flat energy distribution of $\overline{\rm p}$ up to 25 eV before capture gives $f \approx 4\%$ for helium, independent of the reduced mass of the $\overline{\rm p}{\rm He}^+$ system [5].

Acknowledgements

We are indebted to the LEAR and PS staff at CERN for their tireless dedication in providing us with the high-quality antiproton beam. We would like to thank M. Arzberger for his help during the experiment. We are very grateful to K. Ohtsuki, I. Shimamura and V.I. Korobov for many valuable discussions and theoretical results. The present work is supported by the Grants-in-Aid for Specially Promoted Research and for International Scientific Research of the Japanese Ministry of Education, Science and Culture, the Japan Society for the Promotion of Science (JSPS), the Bundesministerium für Forschung und Technologie and the Hungarian National Science Foundation. F. E. M. acknowledges the receipt of an INOUE fellowship.

T [K]	p [mbar]	ϱ_{mol} [10^{-4} mol/cm^3]	f [%]	$T_{\mathrm{av}}(2\ \mu\mathrm{s})$ [μs]	λ_1 [$\mu\mathrm{s}^{-1}$] 3-level model	λ_3 [$\mu\mathrm{s}^{-1}$]	λ_1 [$\mu\mathrm{s}^{-1}$] 4-level model	λ_4 [$\mu\mathrm{s}^{-1}$]
5.83(20)	204.5(21)	4.28(16)	0.320(4)	3.48(12)	0.404(8)	1.150(75)	0.556(12)	3.46(45)
4.81(18)	193.5(7)	4.95(19)	0.594(5)	3.41(7)	0.411(4)	1.206(46)	0.551(7)	2.76(18)
5.86(18)	402.7(56)	8.52(30)	—	3.34(2)	0.401(1)	1.414(14)	0.529(2)	2.602(41)
5.83(14)	406.3(54)	8.65(25)	—	3.36(1)	0.400(1)	1.428(7)	0.521(1)	2.448(19)
5.83(17)	409(16)	8.70(43)	—	3.35(2)	0.402(1)	1.401(15)	0.527(2)	2.488(43)
5.83(13)	409.5(4)	8.72(20)	2.217(19)	3.38(8)	0.406(4)	1.347(48)	0.521(9)	2.13(12)
5.83(13)	409.8(4)	8.72(20)	2.235(10)	3.38(4)	0.402(2)	1.451(28)	0.526(4)	2.561(75)
5.83(13)	552.1(5)	11.89(28)	—	3.37(2)	0.399(1)	1.655(20)	0.507(3)	2.511(43)
5.83(14)	552.7(7)	11.90(30)	2.369(10)	3.37(4)	0.403(2)	1.574(31)	0.516(4)	2.482(69)
5.83(13)	553.0(20)	11.91(28)	—	3.34(2)	0.401(1)	1.624(15)	0.513(2)	2.514(33)
5.83(16)	565.5(69)	12.19(38)	2.368(7)	3.37(3)	0.401(1)	1.613(21)	0.508(3)	2.421(44)
5.83(10)	566.5(87)	12.22(29)	—	3.36(1)	0.399(1)	1.655(13)	0.508(2)	2.535(27)

Table 1: Summary of target conditions, trapping fractions, average lifetimes and fitted decay rates for low temperature pure ^{3}He measurements. The errors quoted for temperature and pressure arise from fluctuations in time around the mean value, caused by our feedback stabilizing system.

T [K]	p [mbar]	ϱ_{mol} [10^{-4} mol/cm^3]	f [%]	$T_{\mathrm{av}}(2.3\ \mu\mathrm{s})$ [μs]	λ_1 [$\mu\mathrm{s}^{-1}$] 3-level model	λ_3 [$\mu\mathrm{s}^{-1}$]	λ_1 [$\mu\mathrm{s}^{-1}$] 4-level model	λ_4 [$\mu\mathrm{s}^{-1}$]
5.83(10)	204.2(3)	4.30(8)	1.094(9)	4.05(8)	0.383(7)	0.576(15)	0.487(8)	1.006(65)
5.82(19)	404.5(19)	8.73(30)	2.866(11)	3.88(4)	0.387(3)	0.587(7)	0.468(5)	0.795(24)
5.83(10)	425.1(15)	9.18(17)	—	3.88(3)	0.383(2)	0.609(5)	0.452(5)	0.762(17)
10.26(12)	805.8(42)	9.64(13)	2.931(9)	3.87(3)	0.381(2)	0.621(5)	0.447(5)	0.759(18)
5.02(12)	392.1(5)	9.98(25)	2.942(10)	3.88(3)	0.383(2)	0.616(6)	0.457(5)	0.795(19)
5.83(10)	548(17)	12.01(46)	—	3.85(2)	0.376(1)	0.668(4)	0.442(3)	0.820(12)
10.26(12)	1000.0(8)	12.02(14)	2.943(10)	3.86(3)	0.371(2)	0.706(7)	0.429(6)	0.833(20)
10.26(11)	1002.0(10)	12.04(13)	2.937(12)	3.84(4)	0.378(3)	0.684(8)	0.449(6)	0.855(25)
5.83(18)	559.7(24)	12.28(41)	2.874(19)	3.78(6)	0.392(4)	0.669(13)	0.469(10)	0.862(40)
5.82(18)	560.0(23)	12.31(41)	2.926(19)	3.85(6)	0.388(4)	0.671(13)	0.468(8)	0.888(37)
5.82(18)	560.2(23)	12.31(41)	2.932(20)	3.81(6)	0.390(4)	0.692(13)	0.467(9)	0.889(40)
5.82(18)	560.2(21)	12.31(41)	2.870(45)	3.78(14)	0.396(11)	0.699(32)	0.461(70)	0.84(16)
10.27(11)	1041.0(1)	12.51(14)	2.873(29)	3.95(10)	0.378(6)	0.759(23)	0.457(14)	0.983(66)
10.26(10)	1041.0(1)	12.52(13)	2.922(10)	3.82(3)	0.373(2)	0.755(7)	0.443(5)	0.932(20)
5.83(18)	609.8(38)	13.46(46)	2.928(10)	3.86(3)	0.372(2)	0.699(7)	0.443(6)	0.872(21)
5.83(10)	644.1(60)	14.27(30)	—	3.89(3)	0.367(2)	0.722(8)	0.432(6)	0.874(22)
5.02(12)	601.3(11)	15.89(42)	2.911(11)	3.85(4)	0.367(2)	0.775(9)	0.433(6)	0.941(24)
5.83(18)	806.2(39)	18.24(63)	2.900(11)	3.85(4)	0.362(2)	0.868(10)	0.432(6)	1.071(25)
5.02(12)	826.7(73)	22.89(69)	2.884(16)	3.88(5)	0.354(3)	0.995(18)	0.438(6)	1.328(42)
5.82(17)	1009.0(45)	23.54(80)	2.881(14)	3.91(5)	0.349(2)	1.015(15)	0.420(6)	1.273(35)
5.82(18)	1041.0(1)	24.40(87)	2.854(12)	3.86(4)	0.350(2)	1.166(17)	0.427(5)	1.503(35)
5.02(12)	986.0(49)	28.36(87)	2.838(19)	3.86(6)	0.357(3)	1.070(24)	0.448(7)	1.476(52)
5.02(12)	990.4(29)	28.51(86)	2.927(41)	3.84(13)	0.362(7)	1.230(60)	0.435(20)	1.53(12)
5.02(13)	992.0(23)	28.57(93)	2.878(11)	3.90(4)	0.348(2)	1.121(15)	0.431(4)	1.498(33)

Table 2: Summary of target conditions, trapping fractions, average lifetimes and fitted decay rates for low temperature pure ^{4}He measurements. The errors for T and p are due to fluctuations in time around the mean value.

References

[1] M. Iwasaki, S.N. Nakamura, K. Shigaki, Y. Shimizu, H. Tamura, T. Ishikawa, R.S. Hayano, E. Takada, E. Widmann, H. Outa, M. Aoki, P. Kitching and T. Yamazaki, Phys. Rev. Lett. **67**, 1246 (1991).

[2] R.S. Hayano, M. Iwasaki, T. Yamazaki, in *Perspectives of Meson Science* (eds. T. Yamazaki, K. Nakai and K. Nagamine, North-Holland, Amsterdam, 1992), p.417.

[3] T. Yamazaki, E. Widmann, R.S. Hayano, M. Iwasaki, S.N. Nakamura, K. Shigaki, F.J. Hartmann, H. Daniel, T. von Egidy, P. Hofmann, Y.-S. Kim and J. Eades, Nature **361**, 238 (1993).

[4] S.N. Nakamura, R.S. Hayano, M. Iwasaki, K. Shigaki, E. Widmann, T. Yamazaki, H. Daniel, T. von Egidy, F.J. Hartmann, P. Hofmann, Y.-S. Kim, and J. Eades, Phys. Rev. **A49**, 4457 (1994).

[5] T. Yamazaki and K. Ohtsuki, Phys. Rev. **A45**, 7782 (1992).

[6] G.T. Condo, Phys. Lett. **9**, 65 (1964).

[7] J.E. Russell, Phys. Rev. Lett. **23**, 63 (1969); Phys. Rev. **188**, 187 (1969); Phys. Rev. **A1**, 721, 735, 742 (1970); J. Math. Phys. **12**, 1906 (1971); Phys. Rev. **A6**, 2488 (1972).

[8] E. Widmann, I. Sugai, T. Yamazaki, R. S. Hayano, M. Iwasaki, S.N. Nakamura, H. Tamura, T.M. Ito, A. Kawachi, N. Nishida, W. Higemoto, Y. Ito, N. Morita, F.J. Hartmann, H. Daniel, T. von Egidy, W. Schmid, J. Hoffmann and J. Eades, Phys. Rev. **A51**, 2870 (1995).

[9] N. Morita, M. Kamakura, T. Yamazaki, E. Widmann, H. Masuda, I. Sugai, R.S. Hayano, F.E. Maas, H.A. Torii, F.J. Hartmann, H. Daniel, T. von Egidy, B. Ketzer, W. Müller, W. Schmid, D. Horváth and J. Eades, Phys. Rev. Lett. **72**, 1180 (1994).

[10] R.S. Hayano, F.E. Maas, H.A. Torii, N. Morita, M. Kamakura, T. Yamazaki, H. Masuda, I. Sugai, F.J. Hartmann, H. Daniel, T. von Egidy, B. Ketzer, W. Müller, W. Schmid, D. Horváth, J. Eades, E. Widmann, Phys. Rev. Lett. **73**, 1485 (1994); errata Phys. Rev. Lett. **73**, 3181 (1994).

[11] H.A. Torii, R.S. Hayano, F.E. Maas, N. Morita, M. Kamakura, T. Yamazaki, H. Masuda, I. Sugai, F.J. Hartmann, H. Daniel, T. von Egidy, B. Ketzer, W. Müller, W. Schmid, D. Horváth, J. Eades and E. Widmann, *to be published.*

[12] W. Müller, F.J. Hartmann, R.S. Hayano, B. Ketzer, F.E. Maas, Nucl. Instr. and Meth. A **349**, 307 (1994).

[13] J.E. Kilpatrick, W.E. Keller, E.F. Hammel and N. Metropolis, Phys. Rev. **94**, 1103 (1954).

[14] E. Widmann, H. Daniel, J. Eades, T. von Egidy, F.J. Hartmann, R.S. Hayano, W. Higemoto, J. Hoffmann, T.M. Ito, Y. Ito, M. Iwasaki, A. Kawachi, N. Morita, S.N. Nakamura, N. Nishida, W. Schmid, I. Sugai, H. Tamura and T. Yamazaki, Nucl. Phys. **A558**, 697c-680c (1993).

[15] I. Shimamura, Phys. Rev. **A46**, 3776 (1992).

[16] V.E. Markushin, Second Biennial Workshop on Nucleon-Antinucleon Physics (NAN-93), ITEP, Moscow (1993).

[17] G.Ya. Korenman, International Workshop in Theoretical Physics (NEFIM), Balatonfüred, Hungary (1995).

[18] P.T. Greenland and R. Thürwächter, Hyperfine Interact. **76**, 355 (1993).

[19] R. Ahlrichs, O. Dumbraijs, H. Pilkuhn and H.G. Schlaile, Z. Phys. **A306**, 297 (1982).

[20] V.I. Korobov, private communication (1995).

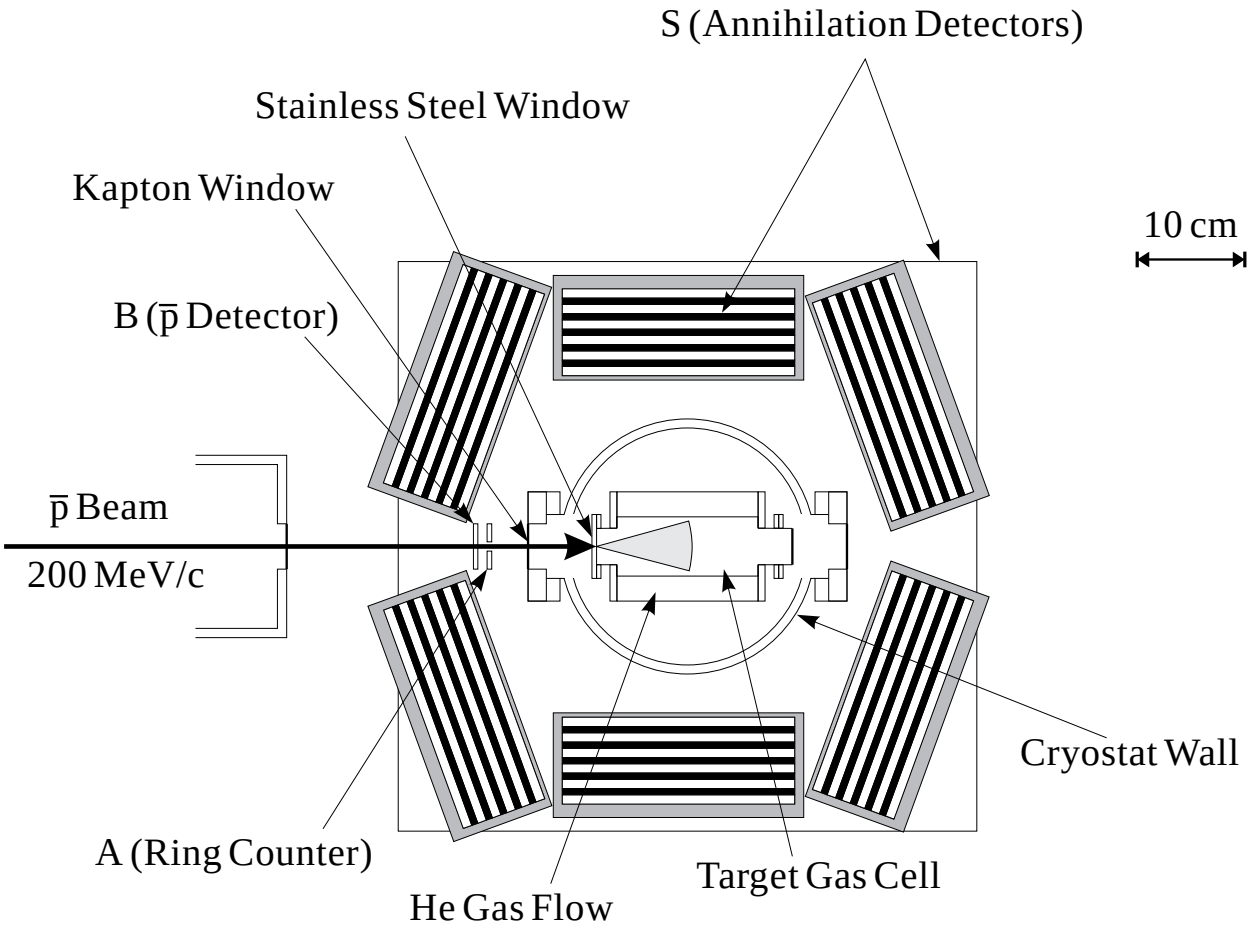

Figure 1: Top view of the experimental setup. The $\overline{p}$, extracted with a momentum of $p = 200$ MeV$/c$, traverse a beam telescope (B and A) before entering the target chamber through a steel window. A liquid helium cryostat keeps the chamber at temperatures between 4.3 K and 10 K. Both charged and neutral annihilation products are detected by seven shower counters S, six of them surrounding the cryostat and one positioned underneath.

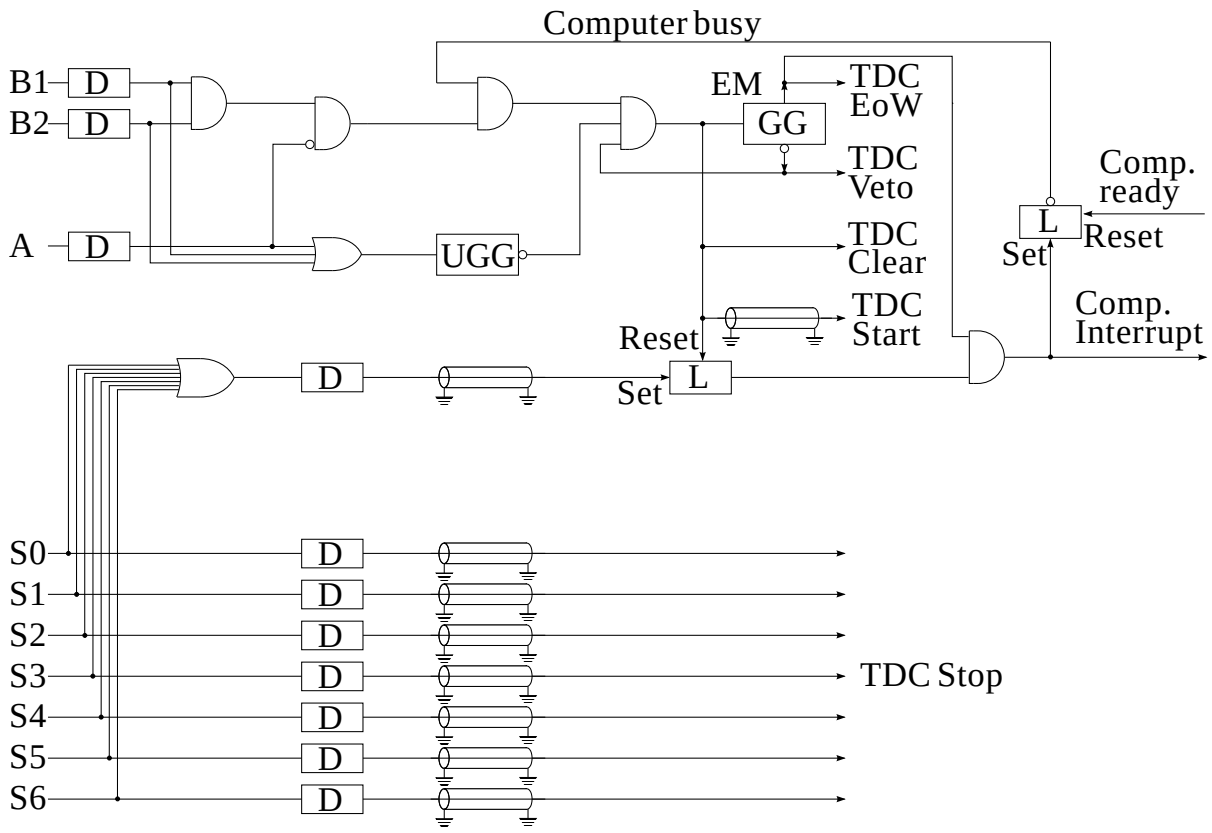

Figure 2: Logic diagram of the electronics. B1 and B2 are the analog signals of two photomultipliers, which detected scintillation light from the beam counter B, A is the ring counter signal and S0 through S6 represent the shower counter signals. The analog signals are then transformed into logic pulses by discriminators D. UGG is an updating 50 μs gate generator, used for pre pile-up rejection, whereas GG generates a 50 μs non updating gate for the TDC window. The End of Window (EoW) signal is given by the End Marker (EM) of this gate generator. Latch modules are abbreviated by L, symbolic coaxial cables represent 500 ns delay lines, respectively.

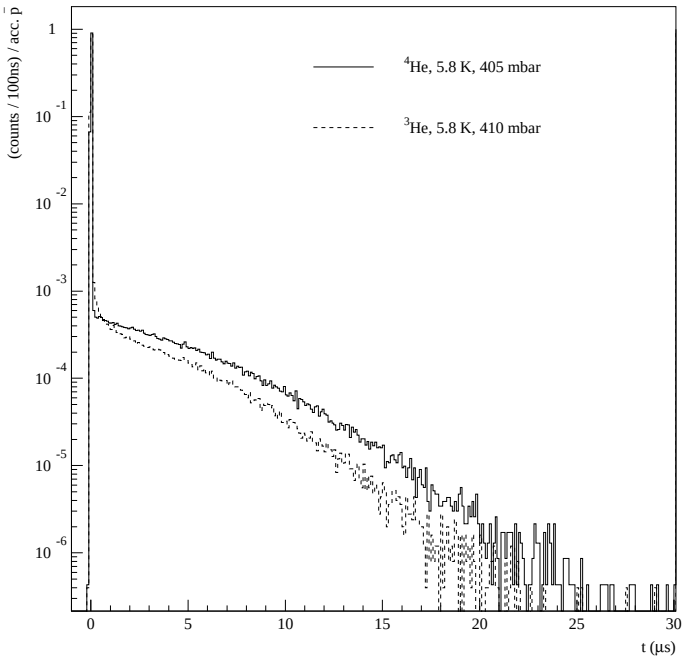

Figure 3: Two typical $\overline{p}$ delayed annihilation time spectra (DATS) from ^{4}He and ^{3}He, showing the downward bent structure in the logarithmic plot, the different overall trapping times of antiprotons and the fast decaying component in the case of ^{3}He.

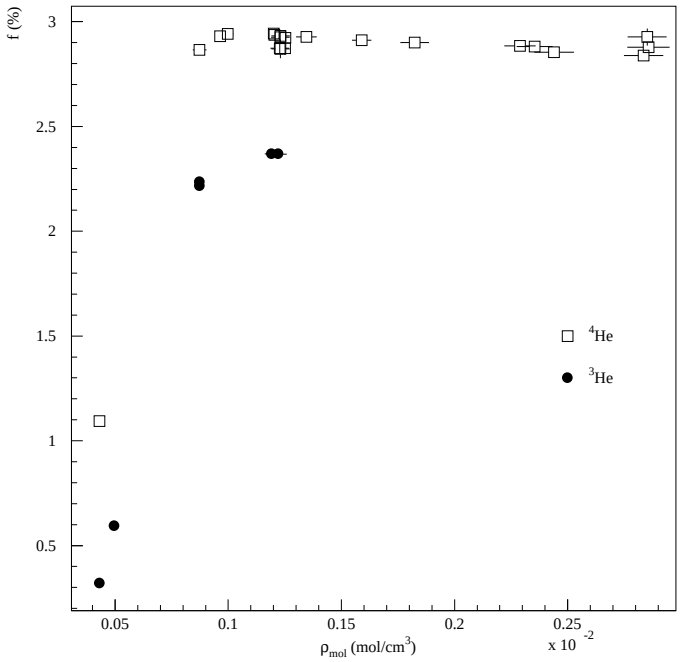

Figure 4: Trapping fraction of antiprotons in ^{3}He and ^{4}He at low pressures as a function of the molar density.

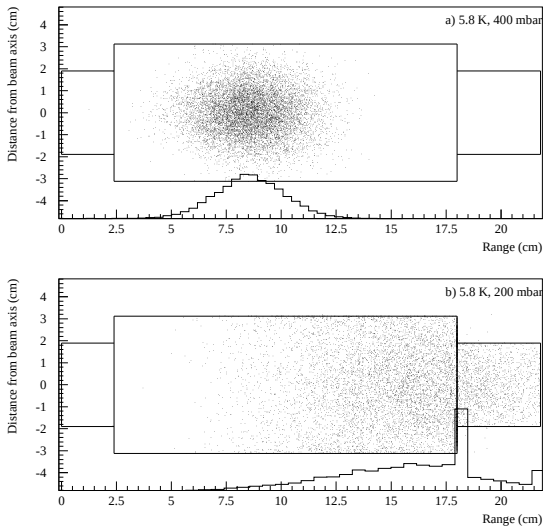

Figure 5: Scatterplot of the calculated stopping distribution of 10000 $\overline{\mathrm{p}}$ in the He target at a) 5.8 K, 400 mbar and b) 5.8 K, 200 mbar. The antiprotons enter the target chamber (indicated by solid lines in the plot, cf. Fig. 1) from the left side. At 400 mbar all antiprotons are stopped in the target gas, while at 200 mbar a large fraction was found to stop in the walls of the target cell, considerably reducing the fraction of delayed annihilations. The projection of the stopping distribution onto the beam axis (range distribution) is shown as a histogram.

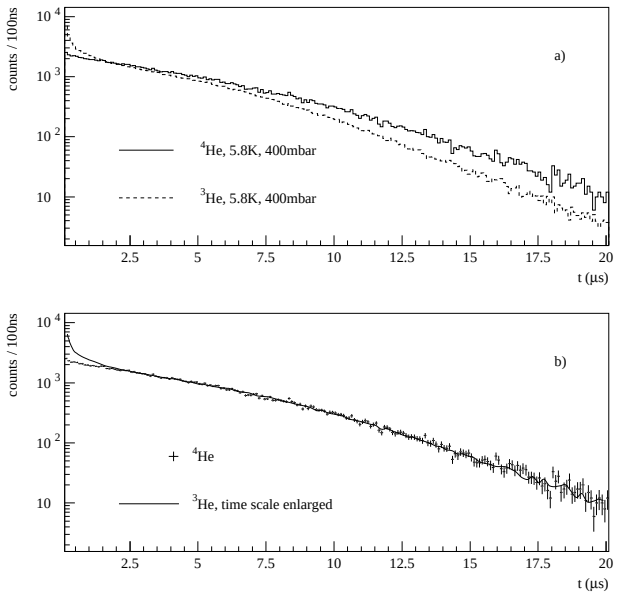

Figure 6: Time spectra of the delayed $\overline{\mathrm{p}}$ annihilation in ^{3}He (solid line) and ^{4}He (dashed line). Figure a) reveals the small difference in the time scale between ^{3}He and ^{4}He DATS for $t > 2\ \mu$s. Figure b) shows the same spectra as Fig. a), with the time scale of the ^{3}He spectrum enlarged by 14.6% (solid line) and the ^{4}He spectrum containing the errors of both spectra.

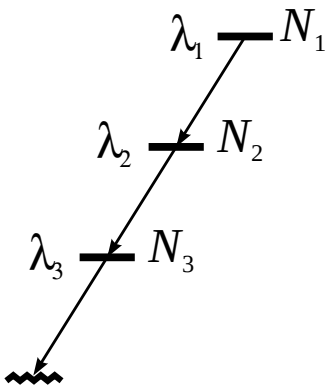

Figure 7: Three-level cascade model. λ_1, λ_2 and λ_3 are the radiative decay rates of the metastable states. N_1, N_2 and N_3 represent the populations of the respective levels.

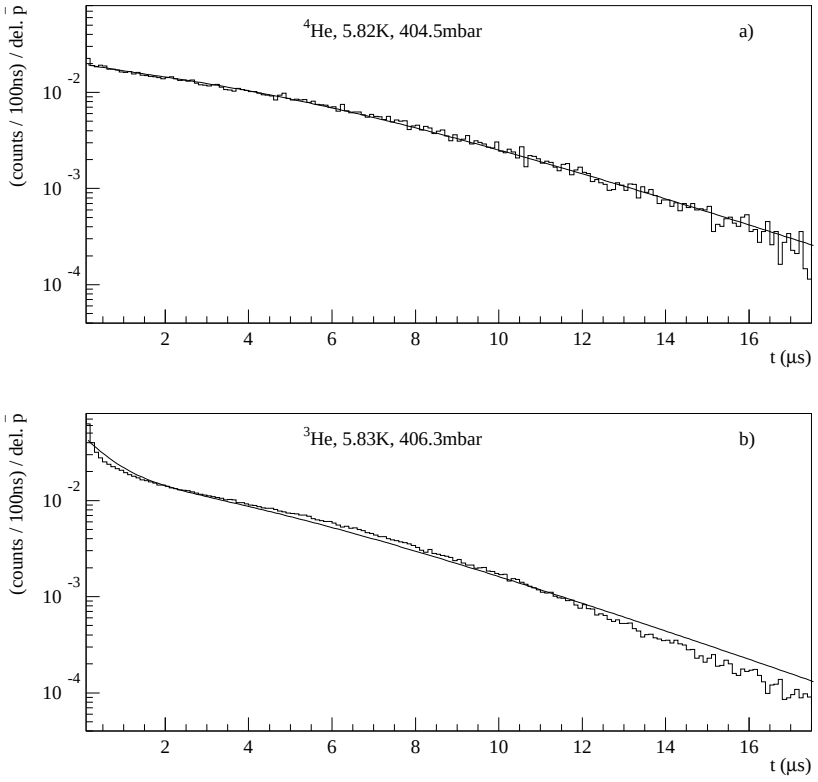

Figure 8: Fits of a three-level model with three free parameters (λ_1, λ_3 and N_0) to the spectra of Fig. 3.

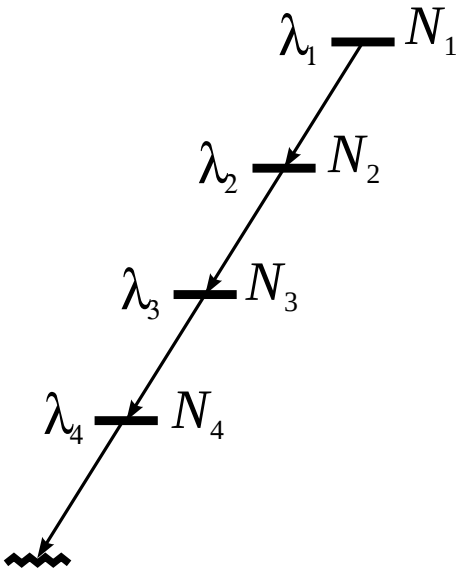

Figure 9: Four-level model of the $\overline{p}$ cascade with decay rates λ_i of the metastable states and level populations N_i, respectively.

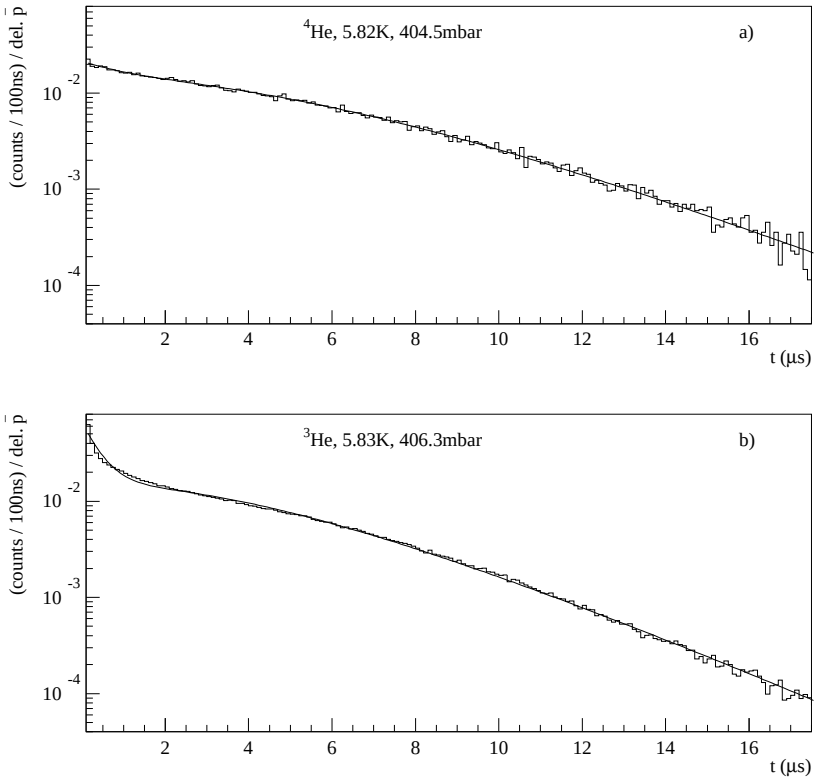

Figure 10: Results of fitting a four-level cascade model with four free parameters to the spectra of Fig. 3.

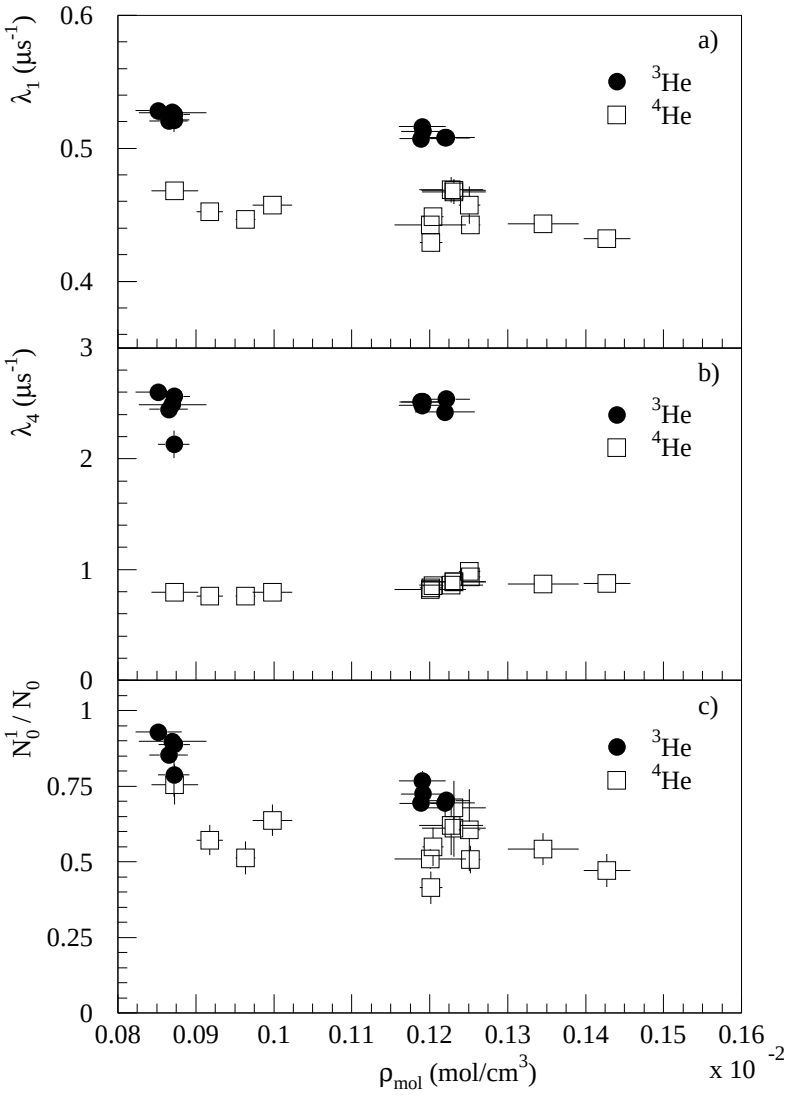

Figure 11: Fit parameters λ_1 (a), λ_4 (b) and N_0^1/N_0 (c) as calculated from the four-level cascade model for ^{3}He and ^{4}He.

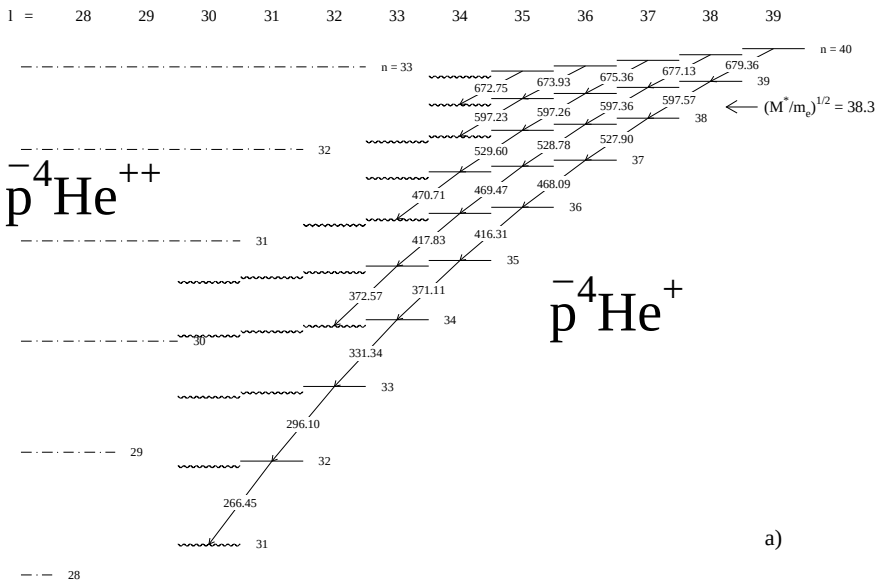

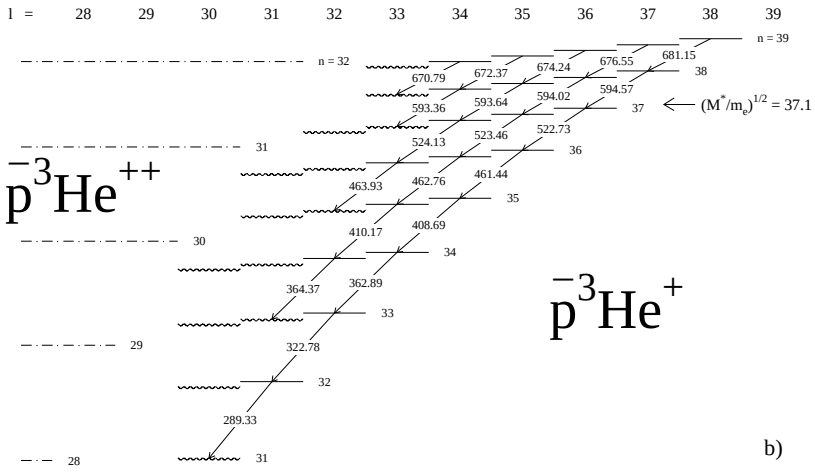

Figure 12: Energy diagrams of $\overline{p}^4He^+$ and $\overline{p}^3He^+$, together with those of $\overline{p}^4He^{++}$ and $\overline{p}^3He^{++}$. The states of $\overline{p}He^+$ are divided into a radiation-dominated metastable zone (bold lines) and a zone of fast-decaying states (zigzag lines), which are expected to decay to states of ionized $\overline{p}He^{++}$ via Auger transitions with $\Delta l \leq 3$. The main radiative cascades are indicated by arrows. The transition wavelengths calculated by Korobov [20] are shown for the relevant transitions, respectively.